



OPEN

Superior asymmetric supercapacitor based on Ni-Co oxide nanosheets and carbon nanorods

SUBJECT AREAS:
BATTERIES
MATERIALS CHEMISTRYReceived
10 September 2013Accepted
16 December 2013Published
16 January 2014Correspondence and
requests for materials
should be addressed to
X.B.Y. (xbyan@licp.
cas.cn)Rutao Wang^{1,2} & Xingbin Yan^{1,3}

¹Laboratory of Clean Energy Chemistry and Materials, Lanzhou Institute of Chemical Physics, Chinese of Academy of Sciences, Lanzhou, 730000, China, ²Graduate University of Chinese Academy of Sciences, Beijing, 100080, China, ³State Key Laboratory of Solid Lubrication, Lanzhou Institute of Chemical Physics, Chinese of Academy of Sciences, Lanzhou, 730000, China.

Nickel and cobalt (Ni-Co) binary oxide nanosheets with mesoporous structure are prepared by a facile approach based on the formation and disassociation of nickel/cobalt-citrate complex, and they show an ultra-high Faradaic capacitance up to 1846 F g⁻¹ and excellent rate capability. On this basic, advanced aqueous asymmetric supercapacitors (AASs) are successfully built by using the Ni-Co oxide as the positive electrode and three kinds of activated carbons respectively as the negative electrode. As-made AASs are able to work reversibly in a full operated voltage region of 0–1.6 V and exhibit outstanding electrochemical performance. Among them, activated polyaniline-derived carbon (APDC)//Ni-Co oxide AASs shows the highest specific capacitance of 202 F g⁻¹, the maximum energy density of 71.7 Wh kg⁻¹, and superior combination of high energy and power density (a energy density of 41.6 Wh kg⁻¹ at a high power density of 16 kW kg⁻¹).

Supercapacitors, also called as electrochemical capacitors, have attracted considerable attention in recent years because they are able to provide high power density (> 10 kW kg⁻¹), long cycle life (> 10⁵ cycles) and fast charge/discharge processes (within seconds)^{1,2}. Currently, they have been widely used in consumer electronics, memory back-up systems, electrical vehicles and industrial power/energy management³. Although supercapacitors have a high power density, they usually suffer from a lower energy density compared with rechargeable batteries⁴. Therefore, it is urgent to develop advanced supercapacitors with enhanced energy density without sacrificing the power delivery and cycle stability. Aqueous asymmetric supercapacitors (AASs), combining a battery-type Faradaic electrode and a capacitor-type electrode, have paid extensive attention as an alternative or supplement to batteries in energy storage field^{1,5–7}. Aqueous electrolytes endow AASs with the advantages of high ionic conductivity, low cost, non-flammability, safety and convenient assembly in air. In addition, AASs can make use of the difference in the potential windows of two electrode materials to increase the maximum operating voltage in the cell system, leading to significantly improve the energy density of devices^{8,9}. Therefore, AASs are able to fill the gap between batteries and conventional capacitors without sacrificing power/energy delivery and cycle life.

To our knowledge, the electrochemical properties of two electrodes directly affect the power and energy density of AASs. For the negative electrode aspect, various carbon materials and metal oxides (such as MoO₃^{10,11}, V₂O₅¹², or FeOOH¹³) are widely studied and contribute to the high energy or power density of AASs. Especially, activated carbon with typical electrochemical double layer capacitance (EDLC) property is used to boost the power density of AASs due to its excellent chemical stability, high rate capacity and acceptable cost^{6,8}. In order to fulfill the demand of high-rate performance at the high current loading, ideal activated carbon materials should have large surface area, open porous structure with well-controlled pore size distribution as well as short pore length, which enable the formation of effective EDLC to facilitate the fast transport of electrolyte ions and large amount of charge storage^{14,15}. As for the positive electrode aspect, various pseudo-capacitive materials, including transition metal hydroxides/oxides and conductive polymers^{2,8,16,17}, are widely used as the positive electrode materials to enlarge the operating voltage and enhance the energy storage capacity due to their desired redox potential and excellent pseudocapacitive properties. In order to fulfill the demand of high energy delivery, ideal positive materials should have the nanostructure and high mesoporosity^{6,18,19}. This is because that the pseudocapacitance is majorly related to fast redox reactions arising from the surface faradic process at an appropriate potential. Smaller size and higher porosity can greatly reduce the diffusion path of electrolyte ions, facilitating ionic motion



and redox reactions. For example, Tang *et al.* synthesized battery-type LiMn_2O_4 nanotubes through a sacrificial template method, which exhibit a fast second-level charge capability²⁰. Recently, various types of AASs, such as graphene// $\text{Ni}(\text{OH})_2$ ⁶, carbon nanotubes// MnO_2 ²¹, activated carbon (AC)// MoO_3 ²², AC// LiMn_2O_4 ²³, have been fabricated and exhibited high energy storage capability. However, these AASs still suffer from the relatively low rate capability. This is mainly due to the poor capacitive performance of positive materials at the high current loading and the corresponding carbon negative materials in a low utilization. Thus, the synergistic effect in energy storage from positive electrode and power delivery from negative electrode is critically limited in these AASs.

An efficient strategy to enhance the rate capability of metal oxide/hydroxide positive materials is incorporating one or two metal ions into them to form multi-metal compounds, such as Ni-Co²⁴⁻²⁷, Co-Al²⁸, Co-Ru²⁹, Co-Mo³⁰, Mn-Co³¹ and Ni-Zn-Co oxides or hydroxides³², which can introduce abundant structural defects and ensure fast redox reactions. Among these materials, nanostructural binary Ni-Co oxide is one of the most promising candidates due to the large theoretical capacitance value (exceeding 2000 F g^{-1}), deep average level of discharge, desired rate capability, and richer redox reactions compared with unitary Ni or Co oxide³³⁻³⁵. More recently, Ni-Co oxide-based AASs, including graphene//Ni-Co oxide and AC//Ni-Co oxide³⁶⁻³⁹, have been fabricated and showed remarkably improved rate capability. However, their energy storage capability is still lower than expected value, probably limiting their practical applications.

Here, we design three advanced AASs using mesoporous Ni-Co oxide nanosheets as positive material and different porous AC (commercial AC, activated graphene (AG) or activated polyaniline-derived carbon (APDC)) as the negative material to simultaneously improve the energy and power density. To this end, Ni-Co oxide nanosheets were firstly synthesized by using a novel approach based on the formation and disassociation of nickel/cobalt-citrate complex. As-prepared Ni-Co oxide possesses mesoporous structure, and exhibit an ultrahigh specific capacitance of 1846 F g^{-1} at a current density of 1 A g^{-1} and good rate performance. Meanwhile, AG sheets and APDC nanorods with high specific surface areas (both exceeding

$2000 \text{ m}^2 \text{ g}^{-1}$) and well-controlled pores were prepared, which show superior capacitive performance (both above 250 F g^{-1}) and better rate performance. The results show that all of three AASs exhibit high electrochemical capacitance and excellent rate capability. Especially, APDC//Ni-Co oxide AAS has an ultra-high energy density of 71.7 Wh kg^{-1} at the power density of 0.4 kW kg^{-1} . Moreover, the energy density still remains 41.6 Wh kg^{-1} even at the high power density of 16 kW kg^{-1} .

Results

Positive electrode materials. In our synthesis, we made use of the formation and disassociation of Ni/Co-citrate complex to synthesize sheet-like Ni-Co hydroxide precursor (Fig. 1a). The advantage of this approach is that mesoporous Ni-Co oxide can be easily obtained through subsequent low temperature calcination, endowing the product with high specific surface area and outstanding electrochemical characteristics. The field emission scanning electron microscopy (SEM) images (Fig. 1b, Fig. 1c, and Supplementary Fig. S1) illustrate the mesoporous Ni-Co oxide particles are composed of abundant nanosheets with the irregular and curly layer morphology. Transmission electron microscopy (TEM) image (Fig. 1d) and annular dark field scanning TEM (ADF-STEM) images (Fig. 1d inset) further reveal that as-made Ni-Co oxide displays intercrossed sheet-like structure with lateral sizes ranging from tens to several hundred nanometers, forming a loose framework with abundant open spaces. The lattice fringes shown in high resolution TEM (HRTEM) image (Fig. 1e) can be indexed to the (311) plane of the NiCo_2O_4 and to the (200) plane of NiO. Supplementary Fig. S2a shows X-ray diffraction (XRD) patterns of Ni-Co hydroxide co-precipitate and the final Ni-Co oxide product. The co-precipitate is a mixture of $\beta\text{-Co}(\text{OH})_2$ (JCPDS #74-2075), $\alpha\text{-Ni}(\text{OH})_2$ (JCPDS #22-0444) and $\beta\text{-Ni}(\text{OH})_2$ (JCPDS #30-0443). The relatively broad and poor-defined diffraction peaks for the Ni-Co oxide indicate the incomplete crystallization of NiCo_2O_4 (JCPDS #73-1704). Also, a sign of NiO (JCPDS #73-1519) appears in this XRD pattern, which is due to the conversion of excess $\text{Ni}(\text{OH})_2$ to NiO during the low temperature calcination. More detailed elemental compositions of as-prepared Ni-Co oxide were further

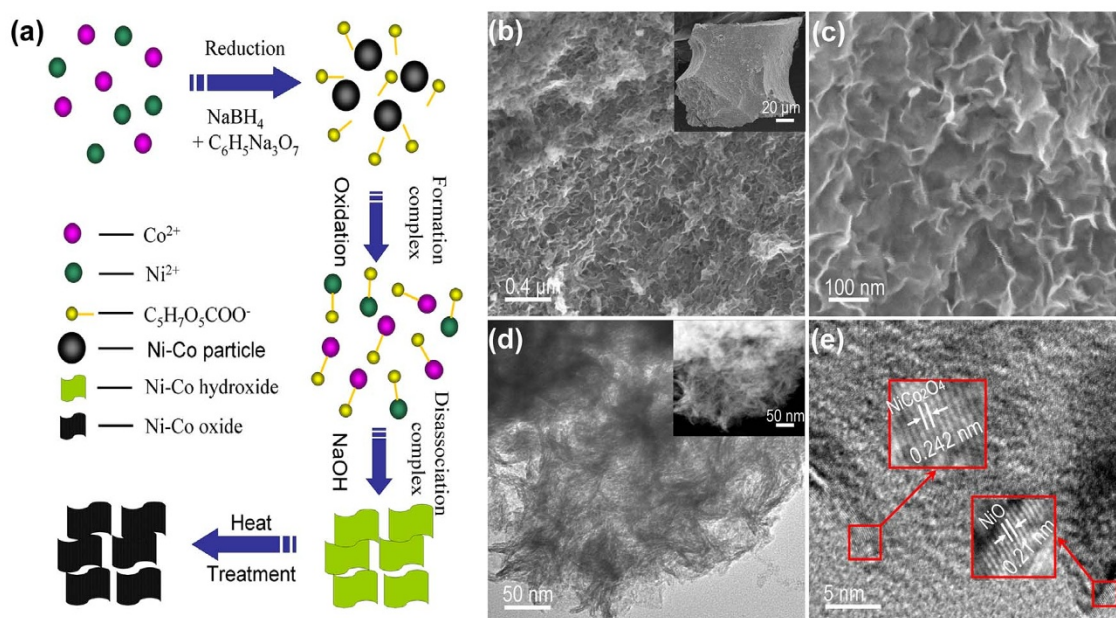


Figure 1 | (a) A schematic show of this facile process of synthesizing Ni-Co oxide nanosheets electrode materials. SEM images (b) and (c), inset image in (b) showing a typical Ni-Co oxide particle. TEM image (d) and the corresponding annular dark field scanning TEM (ADF-STEM) image (inset), and (e) high resolution TEM (HRTEM) image of Ni-Co oxide. The lattice spacing of around 0.242 nm and 0.21 nm are in good agreement of with the data of (311) plane for NiCo_2O_4 and (200) plane for NiO, respectively.



characterized by X-ray photoelectron spectroscopy (XPS) measurement and the corresponding results are present in supplementary Fig. S1b and S1c. By using a Gaussian fitting method, the Ni 2p emission spectrum is fitted with two spin-orbit doublets (supplementary Fig. S2b), characteristic of Ni²⁺ and Ni³⁺, and two shakeup satellites (indicated as 'Sat.')⁴⁰. The Ni²⁺/Ni³⁺ atom ratio obtained from the main lines at 854.7 eV and 856.1 eV is about 0.3, which is close to the value for Ni-Co oxide obtained from the thermal decomposition of nickel and cobalt carbonates⁴¹. As shown in supplementary Fig. S2c, the Co 2p emission spectrum is well fitted with two spin-orbit doublets, characteristic of Co²⁺ and Co³⁺, and two shakeup satellite^{40–44}. The porous characteristics of Ni-Co oxide were investigated by a nitrogen adsorption-desorption measurement and the corresponding isotherm curves are shown in supplementary Fig. S2d. It can be seen that Ni-Co oxide sample gives rise to a type-IV isotherm with an obvious hysteresis loop, indicating the capillary condensation of the mesopores. The sample has a large specific surface area of 207.3 m² g⁻¹ and typical mesoporous structure with the pore size distribution centered at 2.9 nm and 4.6 nm (inset of supplementary Fig. S2d). Such porous characteristics of Ni-Co oxide might be the consequence of the energetically favored phase transformation aspect and strain relaxation in the solid-state oxidative reaction^{40,45}.

Electrochemical properties of the mesoporous Ni-Co oxide were investigated by cyclic voltammetry (CV), galvanostatic charge/discharge (GCD) and electrochemical impedance spectrum (EIS) tests in a three-electrode system and a 2 M KOH electrolyte. The CV curves show a typical pseudocapacitive behavior, having a pair of obvious redox peaks of the voltammetry characteristics (Fig. 2a). The

redox peaks indicate that the capacitive response comes from Faradaic redox reactions related to M-O/M-O-OH (M represents Ni or Co)³³. As shown in Fig. 2b, nearly symmetric potential-time curves at different current densities imply the high charge-discharge coulombic efficiency and low polarization of the mesoporous Ni-Co oxide. The specific capacitances are 1846, 1778, and 1486 F g⁻¹ at the current densities of 1, 2, and 5 A g⁻¹, respectively. Even at a relatively high current density of 10 A g⁻¹, it still remains at 1158 F g⁻¹, thereby exhibiting good rate capability and superior electrochemical capacitance (Fig. 2c). The Nyquist plot (Fig. 2d) ranging from 100 kHz to 0.01 Hz features a high phase-angle (exceeding 45°) impedance plot and a low faradic charge transfer resistance, indicating the fast ion transfer behavior of mesoporous Ni-Co oxide. To the best of our knowledge, such high capacitance performance is rarely observed for electro-active binary Ni-Co oxides^{28,33–39}, which might be attributed to the mesoporous structure and layer-like morphology of the present electrode material.

Negative electrode materials. Porous activated carbon (AC) materials, with high BET surface area and well-controlled pore structure, enable the formation of effective EDLC to facilitate the fast transport of electrolyte ions, and thus can fulfill the demand of high power delivery performance from AASs^{2,6,8}. In this study, three kinds of ACs including commercial AC (see supplementary Fig. S6 and S7), AG and APDC were chosen to combine with as-made mesoporous Ni-Co oxide respectively, to build AASs. As shown in Fig. 3a and Fig. 3b, as-made AG displays irregular shapes with sharp corners, while as-prepared APDC exhibits typical nanorods-like morphology with an average diameter of 100 nm. TEM images highlight that both of

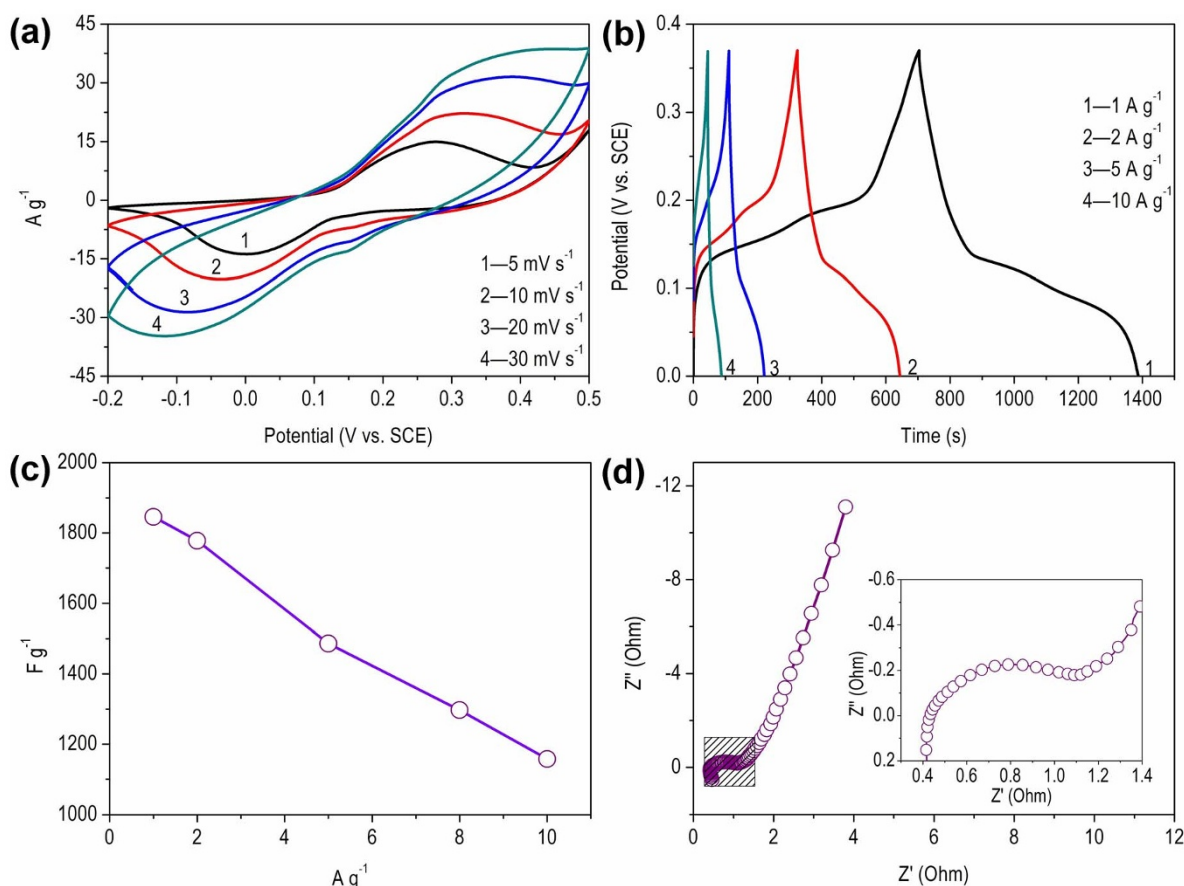


Figure 2 | Electrochemical characteristics of Ni-Co oxide in 2 M KOH aqueous electrolyte under a three-electrode system. (a) CV curves at different scan rates, (b) Galvanostatic charge/discharge curves at different current densities, (c) The specific capacitance as a function of the discharge current density, and (d) Nyquist plot showing the imaginary part versus the real part of impedance. Inset in (d) shows the data of high frequency range (shadow region).



them have highly disordered and dense pores, as shown in Fig. 3c and 3d. As the curves (Fig. 3e) show that, the two samples possess the characteristic type-IV isotherm for mesoporous materials, and the specific surface areas are 2572 and 3353 $\text{m}^2 \text{g}^{-1}$ respectively. The corresponding pore size distributions (Fig. 3f) further reveal the dominant mesopores ranging from 2 nm to 6 nm. In comparison, commercial AC shows a type-I isotherm for microporous characteristic and its specific surface area is about 2203 $\text{m}^2 \text{g}^{-1}$. Its pore sizes are mainly within 1–3 nm. Furthermore, our ACs have larger pore volumes (2.53 $\text{cm}^3 \text{g}^{-1}$ for APDC and 2.08 $\text{cm}^3 \text{g}^{-1}$ for AG, compared to 1.06 $\text{cm}^3 \text{g}^{-1}$ for commercial AC), and higher mesopore percentage (74% for APDC and 68% for AG, compared to 57% for commercial AC).

The electrochemical properties of three ACs were also tested in a three-electrode cell using 2 M KOH electrolyte. All of the ACs show nearly rectangular shaped CV curves, indicating an ideal capacitive behavior, as shown in Fig. 4a and Supplementary Fig. S8. Their charging/discharging curves are relatively linear and symmetrical, also indicating typical characteristic of an ideal supercapacitor (Fig. 4b and Supplementary Fig. S8). Among these ACs, the APDC sample shows the largest CV area and the longest charge/discharge time, which indicates the largest specific capacitance. It can be calculated from the discharge curve with a value of 354 F g^{-1} at the current densities of 1 A g^{-1} . The specific capacitance for AG and AC is about 265 and 279 F g^{-1} , respectively. Even at a relatively high current density of 20 A g^{-1} , both AG and APDC retain more than

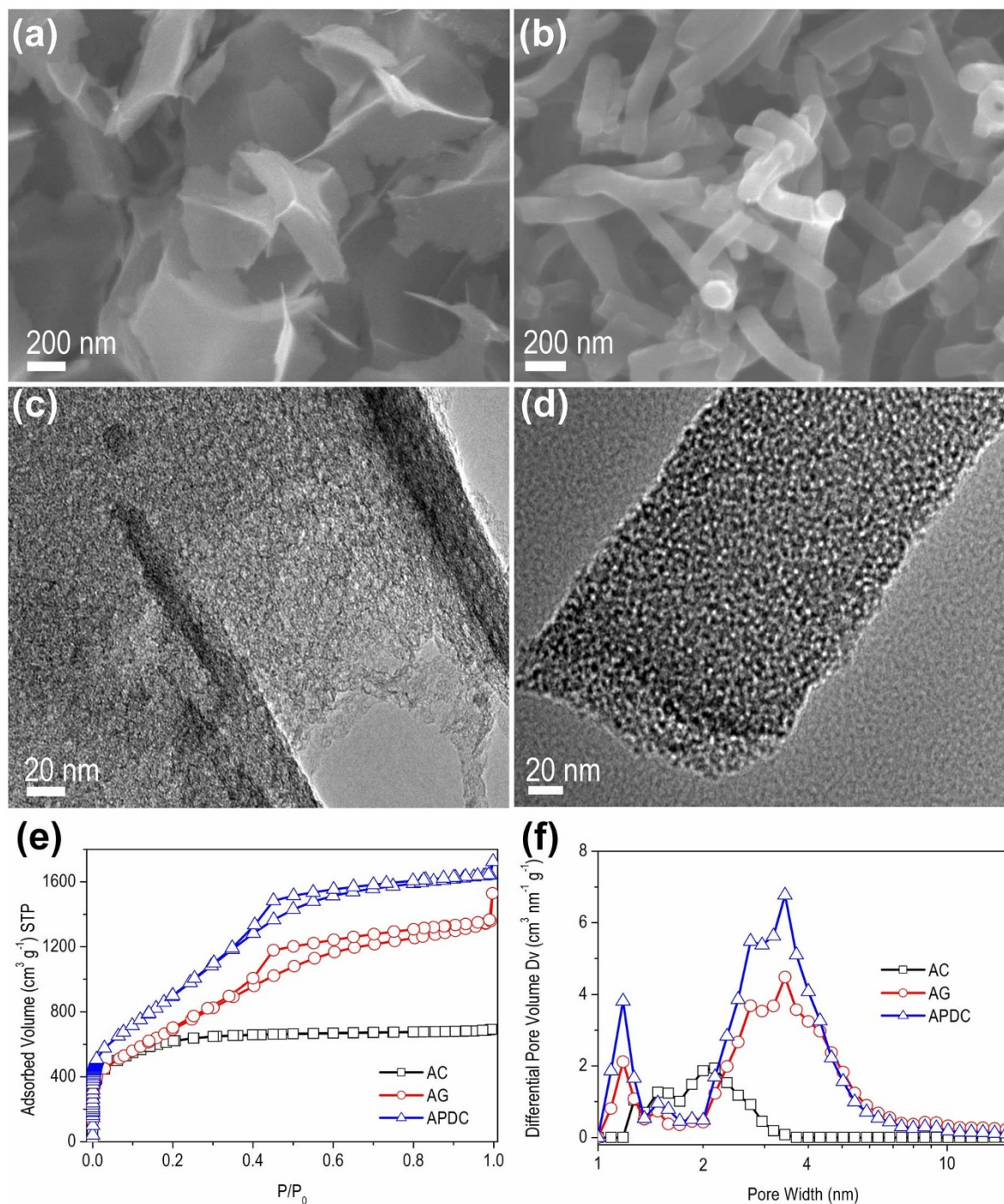


Figure 3 | Morphology and pore structure analysis of as-prepared ACs. SEM images of AG (a) and APDC (c). TEM images of AG (b) and APDC (d). (e) The N_2 sorption isotherms of AG and APDC and commercial AC, and (f) the corresponding pore-size distribution.



74% of their initial capacitances at 1 A g^{-1} , compared with 67.9% for AC (Fig. 4c). Moreover, all of the ACs exhibit outstanding cycle stability with exceeding 80% capacitance retention after 2000 cycles at a high charge/discharge current density of 5 A g^{-1} , as shown in Fig. 4d. These results indicate that three ACs, especially APDC, can deliver high specific capacitance and superior rate ability, making them suitable to pair with as-prepared mesoporous Ni-Co oxide to build advanced AASs.

Advanced AASs based on mesoporous Ni-Co oxide and three ACs.

Three AASs, including AC//Ni-Co oxide, AG//Ni-Co oxide and APDC//Ni-Co oxide, were respectively built by using as-prepared mesoporous Ni-Co oxide as the positive electrode and commercial AC, as-made AG or APDC as the negative electrode. Figure 5a shows the schematic of the assembled structure for such AASs. Figure 5b and Supplementary Figure S9 show the typical CV curves of as-made AASs measured at the different scan rates. Interestingly, the CV curves of AG//Ni-Co oxide and APDC//Ni-Co oxide AASs both exhibit a relatively quasi-rectangular shape. It indicates the fast electrolyte ions transport and redox reaction kinetics for the two AASs due to the excellent synergistic effect of two different energy storage mechanisms. The specific capacitance and rate capability of these AASs were also evaluated by GCD measurements. A good linear relation of the charge/discharge potentials with time is observed (see Fig. 5c and Supplementary Fig. S10), indicating a rapid current-potential response and small equivalent series resistance^{6,46,47}. Furthermore, these curves display the typical triangular shape, demonstrating the excellent electrochemical reversibility and good coulombic efficiency. The specific capacitance is calculated from the discharge curves with values of 144, 150 and 202 F g^{-1} at the current

density of 0.5 A g^{-1} for AC//Ni-Co oxide, AG//Ni-Co oxide and APDC//Ni-Co oxide AASs, respectively. At a relatively high current density of 20 A g^{-1} , the specific capacitance still remain at 71, 80 and 117 F g^{-1} , respectively (Fig. 5d). Furthermore, EIS spectra (Fig. 5e) show that as-fabricated AASs have the low electronic and ionic resistances at high frequencies, a vertical line characteristic of capacitive behavior at low frequencies, and a low time constant (τ_0 , below 10 s), indicating the fast charging/discharging behaviors. In addition, as shown in Fig. 5f, for AG//Ni-Co oxide and APDC//Ni-Co oxide AASs, no serious decay of capacitance is observed after 4000 cycles in KOH electrolyte at a high current density of 5 A g^{-1} , indicating outstanding electrochemical stability. The slight decay of cycle-life for AASs is probably due to the loss of adhesion of active material with the current collector, and the corrosion of current collector caused by the dissolved oxygen in electrolytes during the cycling or matching problems²². Therefore, based on the above investigations, it is revealed that APDC//Ni-Co oxide AAS has the best electrochemical capacitive properties.

Discussion

Figure 6a shows Ragone plots of as-fabricated AASs. As the plots show, the values and change trends of energy and power density for AC//Ni-Co oxide and AG//Ni-Co oxide AASs are very similar, for example, AG//Ni-Co oxide AAS gains a maximum energy density of 53 Wh kg^{-1} at a low power density of 0.4 kW kg^{-1} and it remains 28.3 Wh kg^{-1} at a high power density of 16 kW kg^{-1} . By way of contrast, APDC//Ni-Co oxide AAS gains the maximum energy density of 71.7 Wh kg^{-1} at the power density of 0.4 kW kg^{-1} . This maximum value of energy density is much higher than other reported nickel and/or cobalt-based AASs, such as graphene or

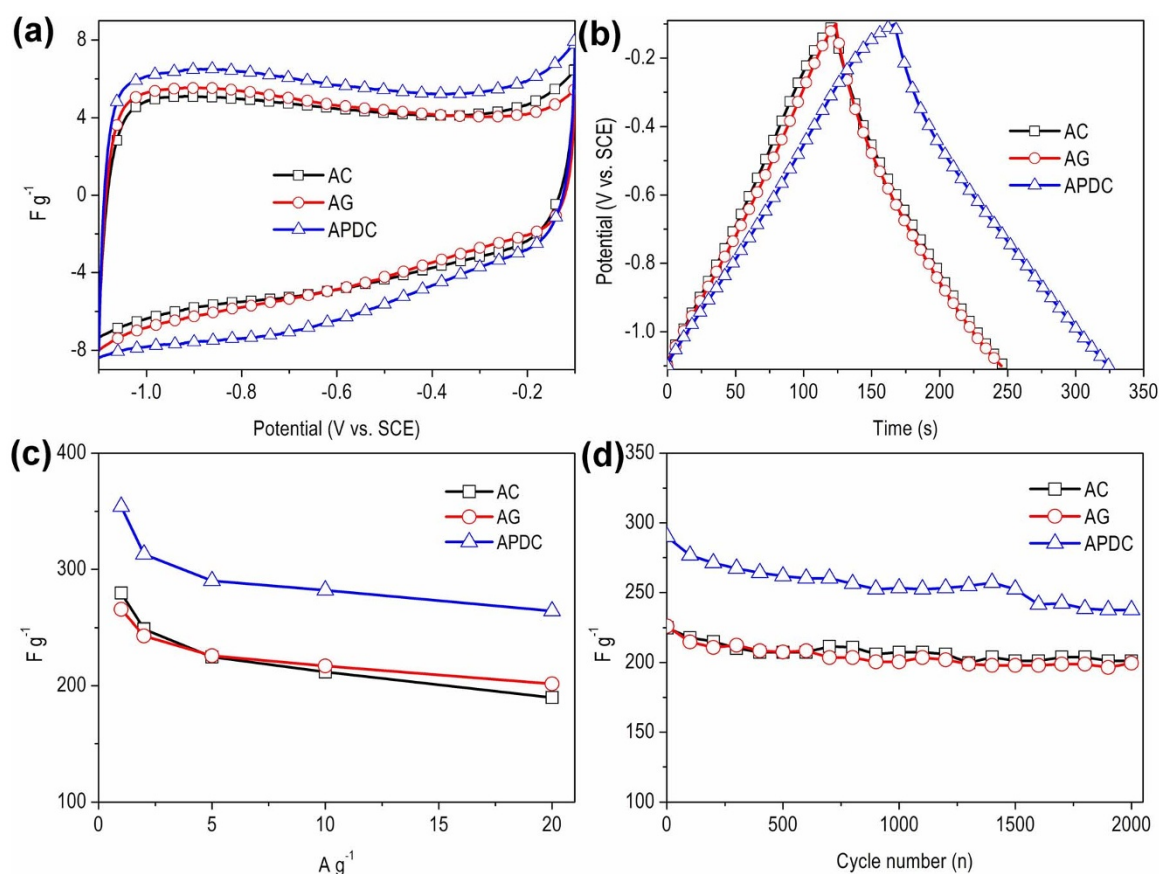


Figure 4 | Electrochemical characteristics of APDC, AG and commercial AC in 2 M KOH aqueous electrolyte under a three-electrode system. (a) CV curves at a scan rate of 20 mV s^{-1} , (b) charging/discharging curves at a current density of 2 A g^{-1} , (c) the specific capacitance as a function of discharge current density, and (d) capacitance retention at the current density of 5 A g^{-1} .

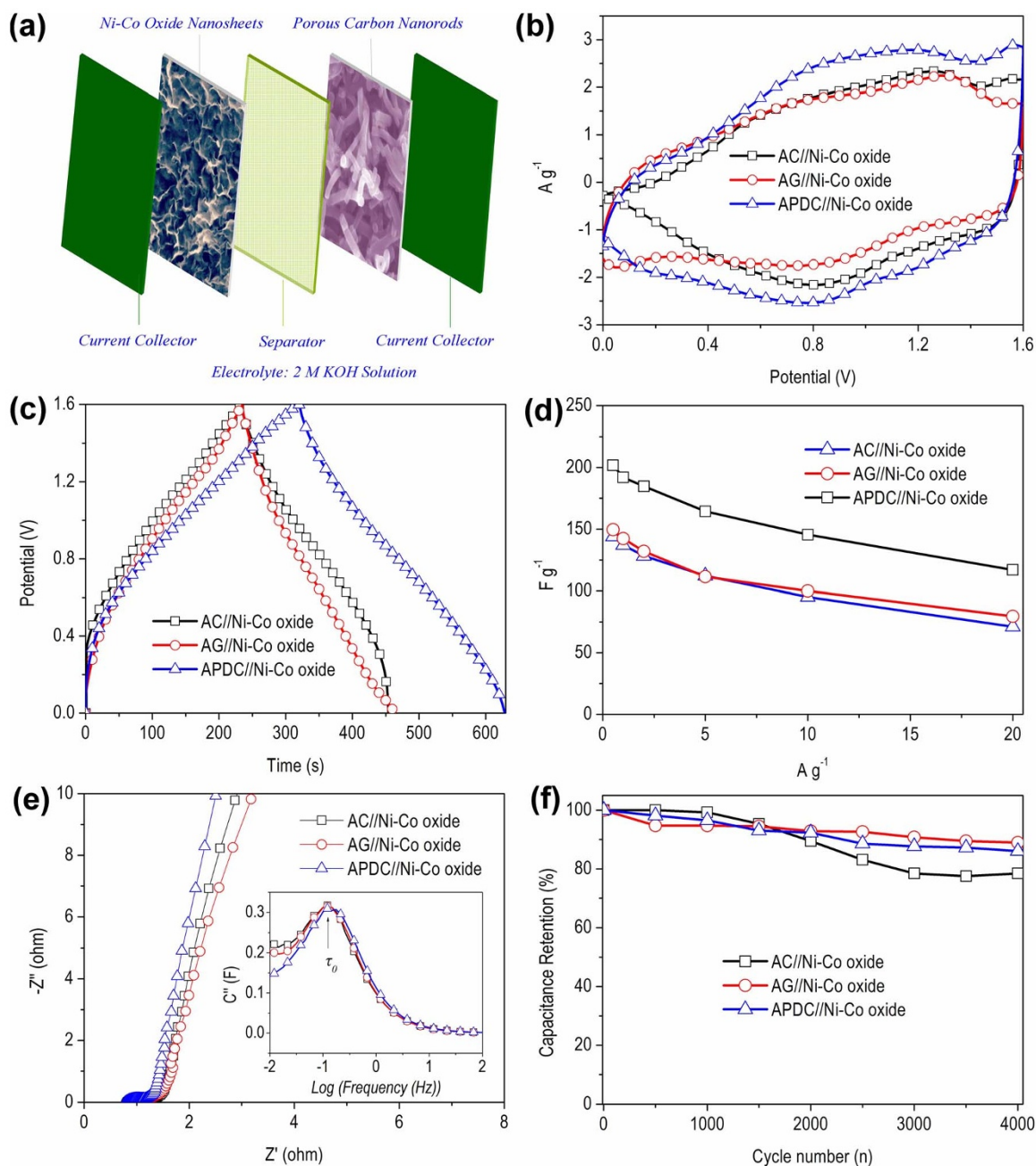


Figure 5 | Electrochemical characteristics of as-fabricated three AASs. (a) Schematic of the assembled structure of AASs based on Ni-Co oxide as the positive electrode and porous carbon as the negative electrode. (b) CV curves at a scan rate of 10 mV s^{-1} , (c) charging/discharging curves at a current density of 1 A g^{-1} , (d) the specific capacitance as a function of discharge current density, (e) EIS plots (inset: imaginary capacitance vs. frequency, τ_0 represents time constant), and (f) capacitance retention at a high current density of 5 A g^{-1} .

AC//Ni(OH)₂ ($35\text{--}52 \text{ Wh kg}^{-1}$)^{48–50}, AC//NiO ($15\text{--}20 \text{ Wh kg}^{-1}$)⁴⁷, AC//Ni-Co oxide ($10\text{--}35 \text{ Wh kg}^{-1}$)^{36–39}, AC//Ni-Zn-Co oxide (41.7 Wh kg^{-1})³², AC//Co(OH)₂ (25.7 Wh kg^{-1})⁵¹, and just a bit lower than reported porous graphene//Ni(OH)₂/graphene (77.8 Wh kg^{-1})⁶. However, it is important to notice that the high energy density for reported porous graphene//Ni(OH)₂/graphene AAS is strongly limited by its relatively low power delivery, for example, the energy density decreases to 13.5 Wh kg^{-1} at a high power density of 15.2 kW kg^{-1} (Fig. 6b). As we know, the most important point for high performance supercapacitors is to obtain a high energy density and meanwhile remaining an outstanding power density. In comparison, our APDC//Ni-Co oxide AAS simultaneously combines the excellent properties of high energy density and high power density.

As shown in Fig. 6b, it still has a high energy density of 41.6 Wh kg^{-1} at the high power density of 16 kW kg^{-1} .

The superior electrochemical performance of the APDC//Ni-Co oxide AAS is mainly attributed to the following aspects: 1) sheet-like mesoporous Ni-Co oxide plays a key role in fabricating the AAS with high energy and power density. Sheet-like morphology and mesoporous structure are able to enrich and shorten the diffusion paths for both electrons and ions in the oxide materials and enhance interfacial redox reactions, resulting in the increase of capacitance and rate capability. In addition, the synergistic effects of nickel and cobalt atoms in Ni-Co oxide is not neglected through modifying their physical properties (thermodynamics and active site density) and spurring a deeper average level of discharge associating to a two

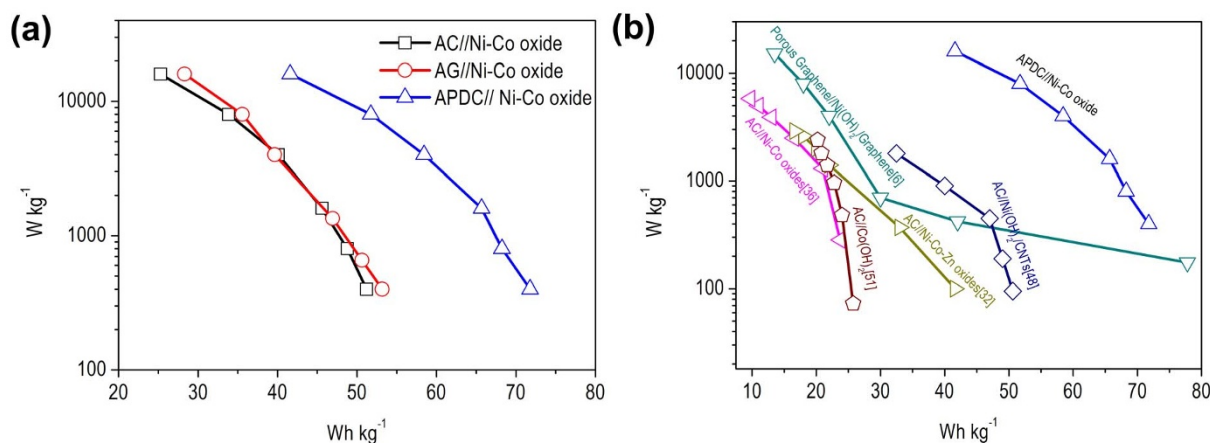


Figure 6 | (a) Ragone plots (energy density vs. power density) of as-made three AASs, and (b) a comparison among as-made APDC//Ni-Co oxide AAS with other reported typical Ni and/or Co-based AASs.

electron-transfer process (two electron redox reactions)⁵². 2) The high surface area and mesoporous structure of APDC are favorable toward forming a large amount of double layers and promoting electrolyte ions intercalation/deintercalation, which both are able to provide enhanced energy storage and good rate capability. Also, mesoporous APDC with nanorod morphology can visually shorten the ionic diffusion paths and thus reduce the ionic diffusion loss owing to the ohmic resistance and electron transfer resistance. Due to that, mesoporous APDC pairing with mesoporous Ni-Co oxide endows the resulting AAS with ideal capacitive behavior. For instance, APDC//Ni-Co oxide AAS shows a quasi-rectangular shape of CV curve and can charge/discharge at a pseudo-constant rate over a full operated voltage. Therefore, based on the above results and discussion, it is a promising way that through increasing the specific capacitance and rate capability of both negative and positive materials to raise the energy and power density of AASs. More recently, Wang and co-workers successfully designed a novel intertwined CNT-MnO₂ hybrid structure on Ni foam, and as-made graphene foam//CNT-MnO₂ ASS shows an extremely high energy density (98 Wh/kg) and power density (200 kW/kg)⁵³. It is mainly due to the novel 3D hierarchical structure and good electrical conductivity of CNT-MnO₂ material, favoring the diffusion and migration of electrolyte ions and consequently improving the effective electrochemical utilization of MnO₂. We believe that, if the Ni-Co oxide nanosheets are anchored on the conductive CNTs, graphene sheets or a 3D conductive framework, their electrochemical performance would be further improved. In the near future, we will work on this issue.

Methods

Synthesis of mesoporous Ni-Co oxide. The preparation of Ni-Co oxide includes a formation and dissociation of complex process followed by a heat treatment step, as shown in Fig. 1a. In a typical synthesis, 0.172 mM of $Co(NO_3)_2 \cdot 6H_2O$, 0.172 mM of $Ni(NO_3)_2 \cdot 6H_2O$ and 1.16 mM of $C_6H_5Na_3O_7 \cdot 2H_2O$ were firstly dissolved in 20 ml of distilled water under magnetic stirring. To this mixture, 10 ml of $NaBH_4$ aqueous solution ($0.1\ mol\ L^{-1}$) was rapidly injected with vigorous stirring, generating a black solution. The whole solution was kept stirring for 2 h at room temperature to promote the complete oxidation of Co and Ni particles and to form stable cobalt/nickel-citrate species, as suggested by the color change of the solution from black to clear. More details about the role of sodium citrate was given in Wang and Kong' work⁵⁴. After that, 5 ml of 4 M NaOH aqueous solution was added to the mixture immediately. The reaction mixture was kept stirring for 5 min and then left undisturbed at 60 °C for 24 h. Finally, a light green solid was obtained, indicating the formation of $Ni(OH)_2/Co(OH)_2$ hybrid precipitation. The precipitation was collected and washed with ethanol and distilled water by centrifugation at 5000 rpm, and dried at 60 °C. After a subsequent thermal treatment at 200 °C in air for 6 h with a heating rate of $2\ ^\circ C\ min^{-1}$, the light green precipitation was changed into black Ni-Co oxide powder. The optimal parameters, such as the Co/Ni molar ratios and calcination temperatures, were discussed in Supplementary Fig. S2–S4.

Synthesis of activated graphene (AG). AG was prepared by a KOH activation approach according to Ruoff' work with a little modification⁵⁵. Briefly, a graphene oxide (GO) aqueous suspension ($5\ mg\ ml^{-1}$) was prepared by sonication of graphite oxide, which was obtained from natural graphite using modified Hummers method. Ten ml of 6 M KOH solution was added into 100 ml of GO suspension under vigorous stirring. The water in the GO/KOH solution was then evaporated using an oil bath at 100 °C under constant stirring until the solution was transformed into dry mixture. The dry mixture was then heated at 800 °C for 1 h under an argon atmosphere. After being cooled down to room temperature, the product was washed with dilute HCl solution and ultrapure water until the pH value of washing water reached 7, and then dried at 60 °C in air.

Synthesis of activated polyaniline-derived carbon (APDC) nanorods. The polyaniline (PANI) nanorods were synthesized by oxidative polymerization of aniline with ammonium per-sulfate in an aqueous solution containing citric acid. A typical process was shown as follows: 10 g of aniline and 10 g of citric acid were mixed in 1000 ml of distilled water. Then, an aqueous solution of ammonium persulfate was rapidly added into the above mixture solution with a vigorous stirring. After 30 s, the stirring was stopped and the resulting solution was left standing for 24 h at 4 °C in a refrigerator. After that, a dark green PANi nanorods suspension with high suspended stability was formed. The PANi nanorods were collected by filter with water and then dried in freezer dryer for 48 h. As-prepared PANi nanorods were then pyrolyzed at 800 °C for 1 h under argon atmosphere to obtain PANi-derived carbon (denoted as PDC). Subsequently, KOH activation was carried out as follows. Typically, 0.4 g of PDC was impregnated with 2.4 g of KOH in aqueous phase with the aid of sonication. After the removal of water, the dried PDC/KOH mixture was heated at 800 °C for 1 h under an argon atmosphere. After being cooled down to room temperature, the product was washed with dilute HCl solution and ultrapure water until the pH value of the washing water reached 7, and then dried at 60 °C in air. The final porous activated PDC nanorods product was designated as APDC.

Structural characterization. Field emission scanning electron microscopy (FESEM, Hitachi S4800) and transmission electron microscopy (TEM, JEOL 2100 FEG) were employed to investigate the microstructure of as-prepared electrode materials. Powder X-ray diffraction (XRD, Rigaku D/Max-2400) was performed using Cu-K α radiation to investigate the structure and composition of the samples. The surface chemical compositions of as-prepared Ni-Co oxide was examined by X-ray photoelectron spectroscopy (XPS, Perkin-Elmer PHI-5702) with 1486.6 eV radiation as the excitation source. Raman spectra of carbon samples were recorded using a micro-Raman spectroscopy (JY-HR800, the excitation wavelength of 532 nm). The nitrogen adsorption-desorption isotherm measurements were performed on a Micromeritics ASAP 2020 volumetric adsorption analyzer at 77 K. The Brunauer-Emmett-Teller (BET) method was utilized to calculate the specific surface area. The pore-size distribution was determined by a nonlocal density functional method using the nitrogen adsorption data, and assuming a slit pore model. The total pore volume was estimated from the amount adsorbed at a relative pressure of $P/P_0 = 0.99$.

Electrode preparation and electrochemical measurements. The working electrodes were prepared as follows: 80 wt % of sample was mixed with 7.5 wt % of acetylene black and 7.5 wt % of conducting graphite in an agate mortar until a homogeneous black powder was obtained. To this mixture, 5 wt % of poly(tetrafluoroethylene) was added with a few drops of ethanol. After briefly allowing the solvent to evaporate, the resulting paste was pressed at 10 MPa to the nickel gauze with a nickel wire for an electric connection. The assembled electrodes were dried for 12 h at 60 °C in air. Each electrode contains about 5 mg of electro-active material and has a geometric surface area of about $1\ cm^2$.



Electrochemical measurements each electrode material were firstly performed using an electrochemical working station (CHI660D, Shanghai, China) in a three-electrode system in 2 M KOH aqueous electrolyte at room temperature. A platinum gauze electrode and a saturated calomel electrode served as the counter electrode and the reference electrode, respectively. The average specific capacitance values were calculated from the galvanostatic discharge curves, using the following equation:

$$C = I / [(dE/dt) \times m] \approx I / [(\Delta E / \Delta t) \times m] (\text{Fg}^{-1}) \quad (1)$$

Where I is constant discharge current, Δt is the time period for a full discharge, m indicates the mass of the corresponding active electrode material, and ΔE represents the voltage change after a full discharge.

A two-electrode cell configuration was used to measure the performances of as-made AASs in 2 M KOH aqueous electrolyte. The loading mass ratio between each carbon materials and Ni-Co oxide was optimized according the specific capacitance calculated from their discharge curves, respectively. It is well known that the optimal mass ratio between the positive and negative electrodes is obtained when the charge (q) is a certain balance between the two electrodes ($q_+ = q_-$). The charge stored by each electrode usually depends on the specific capacitance (C), the work operating voltage (ΔE) and the mass of the electrode (m) following Equation 2:^{6,8}

$$q = C \times \Delta E \times m \quad (2)$$

and in order to meet the demands ($q_+ = q_-$), the mass balancing will be expressed as follows:^{6,8}

$$m_+ / m_- = (C_- \times \Delta E_-) / (C_+ \times \Delta E_+) \quad (3)$$

For example, the Ni-Co oxide and APDC, the optimal mass ratio (positive/negative) between the two electrodes should be close to 0.55. The active materials were homogeneously mixed with PTFE, acetylene black and conducting graphite according to the above stated method, and then were deposited on the current collector (nickel foam, 12 mm diameter). The mass loading of positive electrode (Ni-Co oxide) and negative electrode (APDC) was 2.3 mg and 4.2 mg, respectively. After being dried and pressed at 10 MPa, the electrodes were assembled into a coin cell (2032 style) and separated by a porous nonwoven cloth separator. Aqueous KOH electrolyte (2 M) was used as the electrolyte. The energy density (E) of AASs can be achieved by the specific capacitance (C) and the cell voltage (V) according to the following equation:

$$E = 0.5 C V^2 (\text{Wh kg}^{-1}) \quad (4)$$

The power density (P) of AASs can be achieved by the energy density (E) and the discharging time (t) according to the following equation:

$$P = E/t (\text{W kg}^{-1}) \quad (5)$$

- Simon, P. & Gogotsi, Y. Materials for electrochemical capacitors. *Nat. Mater.* **7**, 845–854 (2008).
- Pandolfo, A. G. & Hollenkamp, A. F. Carbon properties and their role in supercapacitors. *J. Power Sources* **157**, 11–27 (2006).
- Zhai, Y. *et al.* Carbon materials for chemical capacitive energy storage. *Adv. Mater.* **22**, 4828–4850 (2011).
- Dunn, B., Kamath, H. & Tarascon, J. M. Electrical energy storage for the grid: A battery of choices. *Science* **334**, 928–935 (2011).
- Naoui, K., Ishimoto, S., Miyamoto, J. & Naoui, W. Second generation ‘nanohybrid supercapacitor’: Evolution of capacitive energy storage devices. *Energy Environ. Sci.* **5**, 9363–9373 (2012).
- Yan, J. *et al.* Advanced asymmetric supercapacitors based on Ni(OH)₂/graphene and porous graphene electrodes with high energy density. *Adv. Funct. Mater.* **22**, 2632–2641 (2012).
- Wang, F. *et al.* Electrode materials for aqueous asymmetric supercapacitors. *RSC Adv.* **3**, 13059–13084 (2013).
- Fan, Z. *et al.* Asymmetric supercapacitors based on graphene/MnO₂ and activated carbon nanofiber electrodes with high power and energy density. *Adv. Funct. Mater.* **21**, 2366–2375 (2011).
- Long, J. W. *et al.* Asymmetric electrochemical capacitors—stretching the limits of aqueous electrolytes. *MRS. Bull.* **36**, 513 (2011).
- Chang, J. *et al.* Asymmetric supercapacitors based on graphene/MnO₂ nanospheres and graphene/MoO₃ nanosheets with high energy density. *Adv. Funct. Mater.* **23**, 5074–5083 (2013).
- Liu, Y. *et al.* Polypyrrole-coated α-MoO₃ nanobelts with good electrochemical performance as anode materials for aqueous supercapacitors. *J. Mater. Chem. A* **1**, 13582–13587 (2013).
- Qu, Q., Zhu, Y., Gao, X. & Wu, Y. Core-shell structure of polypyrrole grown on V₂O₅ nanoribbon as high performance anode material for supercapacitors. *Adv. Energy Mater.* **2**, 950–955 (2012).
- Jin, W. H., Gao, G. T. & Sun, J. Y. Hybrid supercapacitor based on MnO₂ and columned FeOOH using Li₂SO₄ electrolyte solution. *J. Power Sources* **175**, 686–691 (2008).
- Zhang, L. L. & Zhao, X. S. Carbon-based materials as supercapacitor electrodes. *Chem. Soc. Rev.* **38**, 2520–2531 (2009).
- Chmiola, J. *et al.* Anomalous increase in carbon capacitance at pore sizes less than 1 nanometer. *Science* **313**, 1760–1763 (2006).
- Cheng, Y. *et al.* Synergistic effects from graphene and carbon nanotubes enable flexible and robust electrodes for high-performance supercapacitors. *Nano Lett.* **12**, 4206 (2012).
- Lu, X., Ma, R., Bando, Y. & Sasaki, T. A general strategy to layered transition-metal hydroxide nanocones: Tuning the composition for high electrochemical performance. *Adv. Mater.* **24**, 2148–2153 (2012).
- Zhang, G. & Lou, X. W. Controlled growth of NiCo₂O₄ nanorods and ultrathin nanosheets on carbon nanofibers for high-performance supercapacitors. *Sci. Rep.* **3**, 1470 (2012).
- Brezesinski, T., Wang, J., Tolbert, S. H. & Dunn, B. Ordered mesoporous α-MoO₃ with iso-oriented nanocrystalline walls for thin-film pseudocapacitors. *Nat. Mater.* **9**, 146–151 (2010).
- Tang, W. *et al.* LiMn₂O₄ Nanotube as cathode material of second-level charge capability for aqueous rechargeable batteries. *Nano Lett.* **13**, 2036–2040 (2013).
- Jiang, H., Li, C. Z., Sun, T. & Ma, J. A green and high energy density asymmetric supercapacitor based on ultrathin MnO₂ nanostructures and functional mesoporous carbon nanotube electrodes. *Nanoscale* **4**, 807–812 (2012).
- Tang, W. *et al.* Aqueous supercapacitors of high energy density based on MoO₃ nanoplates as anode material. *Chem. Commun.* **47**, 10058–10060 (2011).
- Wang, Y. G. & Xia, Y. Y. Hybrid aqueous energy storage cells using activated carbon and lithium-intercalated compounds. I. The C/LiMn₂O₄ system. *J. Electrochem. Soc.* **153**, A450–A454 (2006).
- Wei, T. Y. *et al.* A cost-effective supercapacitor material of ultrahigh specific capacitances: Spinel nickel cobaltite aerogels from an epoxide-driven sol-gel process. *Adv. Mater.* **22**, 347–351 (2010).
- Wu, H. B., Pang, H. & Lou, X. W. Facile synthesis of mesoporous Ni_{0.3}Co_{2.7}O₄ hierarchical structures for high-performance supercapacitors. *Energy Environ. Sci.* **6**, 3619–3262 (2013).
- Zhang, G. Q. *et al.* Single-crystalline NiCo₂O₄ nanoneedle arrays grown on conductive substrates as binder-free electrodes for high-performance supercapacitors. *Energy Environ. Sci.* **5**, 9453–9456 (2012).
- Zhang, G. & Lou, X. W. General solution growth of mesoporous NiCo₂O₄ nanosheets on various conductive substrates as high-performance electrodes for supercapacitors. *Adv. Mater.* **25**, 976–979 (2013).
- Wang, Y. G., Cheng, L. & Xia, Y. Y. Electrochemical profile of nano-particle CoAl double hydroxide/active carbon supercapacitor using KOH electrolyte solution. *J. Power Sources* **153**, 191–196 (2006).
- Xu, J. *et al.* Flexible asymmetric supercapacitors based upon Co₉S₈ nanorod//Co₃O₄@RuO₂ nanosheet arrays on carbon cloth. *ACS Nano* **7**, 5453–5462 (2013).
- Mai, L. Q. *et al.* Hierarchical MnMoO₄/CoMoO₄ heterostructured nanowires with enhanced supercapacitor performance. *Nat. Commun.* **2**, 381 (2011).
- Liu, J. *et al.* Co₃O₄ Nanowire/MnO₂ ultrathin nanosheet core/shell arrays: A new class of high-performance pseudocapacitive materials. *Adv. Mater.* **23**, 2076–2081 (2011).
- Wang, H., Gao, Q. & Hu, J. Asymmetric capacitor based on superior porous Ni-Zn-Co oxide/hydroxide and carbon electrodes. *J. Power Sources* **195**, 3017–3024 (2010).
- Yuan, C. *et al.* Ultrathin mesoporous NiCo₂O₄ nanosheets supported on Ni foam as advanced electrodes for supercapacitors. *Adv. Funct. Mater.* **22**, 4592–4597 (2012).
- Xia, X. *et al.* High-quality metal oxide core/shell nanowire arrays on conductive substrates for electrochemical energy storage. *ACS Nano* **6**, 5531–5538 (2012).
- Wang, H., Gao, Q. & Jiang, L. Facile approach to prepare nickel cobaltite nanowire materials for supercapacitors. *Small* **7**, 2454–2459 (2011).
- Wang, H. *et al.* Graphene-nickel cobaltite nanocomposite asymmetrical supercapacitor with commercial level mass loading. *Nano Res.* **5**, 605–617 (2012).
- Wang, X., Sumboja, A., Lin, M. F., Yan, J. & Lee, P. S. Enhancing electrochemical reaction sites in nickel-cobalt layered double hydroxides on zinc tin oxide nanowires: a hybrid material for an asymmetric supercapacitor device. *Nanoscale* **4**, 7266–7272 (2012).
- Sun, X. *et al.* Morphology controlled high performance supercapacitor behaviour of the Ni-Co binary hydroxide system. *J. Power Sources* **238**, 150–156 (2013).
- Hsu, H. T. & Hu, C. C. Synthesis and characterization of mesoporous spinel NiCo₂O₄ using surfactant-assembled dispersion for asymmetric supercapacitors. *J. Power Sources* **242**, 662–671 (2013).
- Cui, B. *et al.* Photophysical and photocatalytic properties of core-ring structured NiCo₂O₄ nanoplatelets. *J. Phys. Chem. C* **113**, 14083–14087 (2009).
- Marco, J. F. *et al.* Characterization of the nickel cobaltite, NiCo₂O₄, prepared by several methods: An XRD, XANES, EXAFS, and XPS study. *J. Solid State Chem.* **153**, 74–81 (2000).
- Li, Y., Hasin, P. & Wu, Y. Ni_xCo_{3-x}O₄ nanowire arrays for electrocatalytic oxygen evolution. *Adv. Mater.* **22**, 1926–1929 (2010).
- Choudhury, T., Saied, S. O., Sullivan, J. L. & Abbot, A. M. Reduction of oxides of iron, cobalt, titanium and niobium by low-energy ion bombardment. *J. Phys. D: Appl. Phys.* **22**, 1185–1195 (1989).
- Roginskaya, Y. E. *et al.* Characterization of Bulk and Surface Composition of Co_xNi_{1-x}O_y Mixed Oxides for Electrocatalysis. *Langmuir* **13**, 4621–4627 (1997).
- Li, Y., Tan, B. & Wu, Y. Freestanding mesoporous quasi-single-crystalline Co₃O₄ nanowire arrays. *J. Am. Chem. Soc.* **128**, 14258–14259 (2006).



46. Stoller, M. D., Park, S. J., Zhu, Y., An, J. & Ruoff, R. S. Graphene-based ultracapacitors. *Nano Lett.* **8**, 3498–3502 (2008).
47. Wang, D. W., Li, F. & Cheng, H. M. Hierarchical porous nickel oxide and carbon as electrode materials for asymmetric supercapacitor. *J. Power Sources* **185**, 1563–1568 (2008).
48. Tang, Z., Tang, C. H. & Gong, H. A high energy density asymmetric supercapacitor from nano-architected Ni(OH)₂/carbon nanotube electrodes. *Adv. Funct. Mater.* **22**, 1272–1278 (2012).
49. Li, H. B. *et al.* Amorphous nickel hydroxide nanospheres with ultrahigh capacitance and energy density as electrochemical pseudocapacitor materials. *Nat. Commun.* **4**, 1894 (2013).
50. Ji, J. *et al.* Nanoporous Ni(OH)₂ thin film on 3D ultrathin-graphite foam for asymmetric supercapacitor. *ACS Nano* **7**, 6237–6243 (2013).
51. Kong, L. B., Liu, M., Lang, J. W., Luo, Y. C. & Kang, L. Asymmetric supercapacitor based on loose-packed cobalt hydroxide nanoflake materials and activated carbon. *J. Electrochem. Soc.* **156**, A1000–A1004 (2009).
52. Armstrong, R. D., Briggs, G. W. D. & Charles, E. A. Some effects of the addition of cobalt to the nickel hydroxide electrode. *J. Appl. Electrochem.* **18**, 215–219 (1988).
53. Wang, W. *et al.* Intertwined nanocarbon and manganese oxide hybrid foam for high-energy supercapacitors. *Small* **9**, 3714–3721 (2013).
54. Wang, R. T. *et al.* Mesoporous Co₃O₄ materials obtained from Cobalt–Citrate complex and their high capacitance behavior. *J. Power Sources* **217**, 358–363 (2012).
55. Zhang, L. L. *et al.* Highly conductive and porous activated reduced graphene oxide films for high-power supercapacitors. *Nano Lett.* **12**, 1806–1812 (2012).

Acknowledgments

This work was supported by the Top Hundred Talents Program of Chinese Academy of Sciences, the National Nature Science Foundations of China (21203223) and the Youth Science Foundations of Gansu Province (1107RJYA274).

Author contributions

W.R.T. and Y.X.B. proposed and designed this project together. W.R.T. and Y.X.B. completed the experimental works. W.R.T. and Y.X.B. wrote the main manuscript and SI text and prepared the Figures. All authors reviewed the manuscript.

Additional information

Supplementary information accompanies this paper at <http://www.nature.com/scientificreports>

Competing financial interests: The authors declare no competing financial interests.

How to cite this article: Wang, R.T. & Yan, X.B. Superior asymmetric supercapacitor based on Ni-Co oxide nanosheets and carbon nanorods. *Sci. Rep.* **4**, 3712; DOI:10.1038/srep03712 (2014).



This work is licensed under a Creative Commons Attribution-NonCommercial-NoDerivs 3.0 Unported license. To view a copy of this license, visit <http://creativecommons.org/licenses/by-nc-nd/3.0>